

Direct comparison of brain [^{18}F]FDG images acquired by SiPM-based and PMT-based PET/CT: phantom and clinical studies

Kei Wagatsuma (✉ wagatsuma@pet.tmig.or.jp)

Tokyo Metropolitan Institute of Gerontology <https://orcid.org/0000-0001-7067-9758>

Muneyuki Sakata

Tokyo Metropolitan Institute of Gerontology

Kenji Ishibashi

Tokyo Metropolitan Institute of Gerontology

Akira Hirayama

GE Healthcare

Hirofumi Kawakami

GE Healthcare

Kenta Miwa

International University of Health and Welfare

Yukihisa Suzuki

Tokyo Medical and Dental University

Kenji Ishii

Tokyo Metropolitan Institute of Gerontology

Original research

Keywords: silicon photomultiplier, photomultiplier tube, digital positron emission tomography, image quality, standardized uptake value ratio, statistical image analysis

Posted Date: July 8th, 2020

DOI: <https://doi.org/10.21203/rs.3.rs-25131/v2>

License:   This work is licensed under a Creative Commons Attribution 4.0 International License.

[Read Full License](#)

Version of Record: A version of this preprint was published at EJNMMI Physics on November 23rd, 2020. See the published version at <https://doi.org/10.1186/s40658-020-00337-4>.

Abstract

Background: The silicon photomultiplier-positron emission tomography (SiPM-PET) developed by GE Healthcare has better sensitivity, spatial resolution, and timing resolution than photomultiplier tubes (PMT)-PET. The present study aimed to clarify the advantages of SiPM-PET in ^{18}F -fluoro-2-deoxy-D-glucose (^{18}F FDG) brain imaging in a head-to-head comparison with PMT-PET in phantom and clinical studies.

Methods: Image contrast was calculated from images acquired from a Hoffman 3D brain phantom and image noise and uniformity were calculated from pooled images acquired from a pool phantom using SiPM- and PMT-PET. Sequential PMT-PET and SiPM-PET ^{18}F FDG images were acquired over a period of 10 min from 22 controls and 10 patients. All images were separately normalized to a standard ^{18}F FDG PET template, then mean standardized uptake values (SUV_{mean}) and Z-score were calculated by MIMneuro and CortexID Suite, respectively.

Results: Image contrast, image noise, and uniformity in SiPM-PET changed 19.2%, 3.5%, and -40.0% from PMT-PET, respectively. These physical indices of both PET scanners satisfied the criteria for acceptable image quality published by the Japanese Society of Nuclear Medicine of $> 55\%$, $\leq 15\%$ and ≤ 0.0249 , respectively. The contrast in SiPM-PET was slightly improved using TOF. The SUV_{mean} using SiPM-PET was significantly higher than PMT-PET and did not correlate with a time delay. Z-scores were also significantly higher in images acquired from SiPM-PET (except for the bilateral posterior cingulate) than PMT-PET because the peak signal that was extracted by the calculation of Z-score in CortexID Suite was raised. The area of hypometabolism in statistical maps was reduced and localized by SiPM-PET compared with PMT-PET regardless of whether the images were derived from controls or patients.

Conclusions: The improved spatial resolution and sensitivity of SiPM-PET contributed to better image contrast and uniformity in brain ^{18}F FDG images. The SiPM-PET offers better quality and more accurate quantitation of brain PET images. The SUV_{mean} and Z-score in SiPM-PET was higher than PMT-PET due to improving the PVEs. ^{18}F FDG images acquired using SiPM-PET will help to improve diagnostic outcomes based on statistical image analysis because the SiPM-PET would localize the distribution of glucose metabolism on Z-score maps.

Introduction

Positron emission tomography (PET) has become an important imaging technology for evaluating biochemical and physiological functions and pathological abnormalities (1, 2). Brain imaging with ^{18}F -fluoro-2-deoxy-D-glucose (^{18}F FDG) measures local glucose metabolism as a proxy for neuronal activity, and thus is a powerful tool for differentially diagnosing dementia (3, 4).

Silicon photomultipliers (SiPM) developed by Hamamatsu Photonics K.K. have replaced photomultiplier tubes (PMT) in newer PET detector systems (5). The SiPM is a solid-state photon-counting device comprising 100 – > 10,000 avalanche photodiode pixels in the Geiger-mode. The desirable features of

SiPM comprise good intrinsic timing resolution (< 200 ps, not for clinical use), compact, rugged design, higher gain (similar to that of PMT) and more sensitive photon detection than PMT (5-11). The scintillator size is a dominant factor in the spatial resolution of PET imaging (12). The clinical PET scanner using SiPM is likely to improve the spatial resolution because it has crystals smaller than 4×4 mm (10, 13). The SiPM gain and photon detection efficiency were overvoltage and temperature dependent (14, 15). The SIGNA PET/MR (GE Healthcare, Milwaukee, WI, USA) and Discovery MI (DMI; GE Healthcare) are kept cool ($17^{\circ}\text{C} - 18^{\circ}\text{C}$) with a constant flow of coolant (8). The first commercial SiPM-based PET/computed tomography (CT) was the Discovery MI (DMI; GE Healthcare, Milwaukee, WI, USA), that had a PET axial field-of-view (FOV) of 20 cm, small lutetium-based scintillators (LBS) with a SiPM block design, and timing resolution of 375 ps (16). We showed that the SiPM-PET had good sensitivity as well as spatial and timing resolution in National Electrical Manufacturers Association (NEMA) performance tests. Contrast was better on images acquired from the DMI than the Discovery PET/CT 710 (D710, GE Healthcare) that had PMT detectors (17).

The clinical applicability of SiPM-PET/CT has been investigated. Hsu et al. found that SiPM-PET improved the contrast recovery of small lesions (16). Tiny malignant lesions in a patient with melanoma were detected on $[^{18}\text{F}]\text{FDG}$ images acquired using SiPM-PET/CT and a Bayesian penalized-likelihood reconstruction algorithm (18). Sonni et al. reported that SiPM technology and time-of-flight (TOF) algorithm could reduce the duration of whole-body image acquisition without loss of the image quality (19). Salvadori et al. compared the image quality of brain $[^{18}\text{F}]\text{FDG}$ images between Philips SiPM- and PMT-PET scanners (20). Image contrast, noise, and spatial resolution were better for images acquired using digital PET in their clinical study. Sluis et al. evaluated the performance of a Siemens SiPM-PET using NEMA tests and visually compared $[^{18}\text{F}]\text{FDG}$ brain images acquired by PMT-PET and SiPM-PET, but did not physically evaluate the quality of $[^{18}\text{F}]\text{FDG}$ brain images (13).

The present study aimed to clarify the advantage of SiPM-PET system in $[^{18}\text{F}]\text{FDG}$ brain imaging in head-to-head comparisons between DMI and D710 in phantom and clinical studies. To our knowledge, this is the first attempt to evaluate the image quality with phantom study and quantitative value and the results of statistical image analysis with clinical study in SiPM-PET.

Materials And Methods

PET/CT systems

Discovery MI

The Discovery MI is a combination of LBS, an SiPM-PET scanner and a 64-slice CT scanner. The LBS includes four blocks of detectors aligned in the axial direction, each comprising 19,584 crystals ($3.95 \times 5.3 \times 25$ -mm) in a 4×9 matrix. The scanner has 36 detector units per ring and 9,792 SiPM channels. The

DMI enables axial and transaxial FOV of 20 and 70 cm, respectively, with 71 image planes spaced at 2.79-mm intervals. The timing resolution is 375 ps (16). The spatial resolution according to NEMA NU 2-2012 is 3.91 mm at full width at half maximum (FWHM) (17).

Discovery PET/CT 710

The Discovery PET/CT 710 is a combination of LBS with PMT-PET and 64-slice CT scanners. The PET scanner has 13,824 LBS crystals in a $4.2 \times 6.3 \times 25\text{-mm}^3$ block. The D710 enables a 150.42-mm axial FOV and a 700-mm transaxial FOV with 47 image planes spaced at 3.27-mm intervals. The timing resolution is 500 ps. The spatial resolution according to a NEMA NU 2-2007 was 4.52 mm at FWHM (21).

PET reconstruction condition

Data acquired using SiPM-PET and PMT-PET were reconstructed under the following conditions: three dimensional-ordered subset-expectation maximization (3D-OS-EM) with TOF; 4 iterations; 16 subsets; Gaussian filter, 2.5 mm (FWHM); 128×128 matrix size; FOV, 25.6 cm; 2.0 mm/pixel. Images of the Hoffman 3D brain phantom acquired by both PET scanners were also reconstructed without TOF to evaluate changes in image contrast using TOF as the contrast gain. The evaluation of contrast gain is described below.

Phantom study

Data acquisition

Images were acquired for 30 min on different days using SiPM-PET and PMT-PET in list mode from a Hoffman 3D brain phantom (Data Spectrum Corporation, Hillsborough, NC, USA) that mimicked the [^{18}F]FDG distribution in the human brain (22) and a pool phantom (Itoi Plastics Co. Ltd., Kobe, Japan), each containing 20 MBq of [^{18}F]FDG. Phantom conditions and the scan duration were determined according to the Japanese Society of Nuclear Medicine (JSNM) phantom test procedure (23). We extracted time frames of 0 – 420 for the PMT-PET and 0 – 380 sec for SiPM-PET from 30 min of data derived from the two phantoms. The count statistics achieved from the PMT-PET time frame were

equivalent to those for [¹⁸F]FDG clinical brain images at our institution as described below. The time frame of SiPM-PET was determined based on radioactive decay during the scan interval during the second acquisition.

Data processing

The physical indices for phantom tests proposed by the JSNM were used to evaluate the image quality: the ratio of gray-to-white matter contrast (contrast, %) calculated from images of Hoffman phantom, image noise (coefficient of variation, CV [%]) and uniformity (standard deviation, SD) calculated from images of pool phantom (23). The SD was also calculated from the pool phantom image with a scan duration of 30 min. The contrast, CV and SD were respectively calculated as described using images acquired from Hoffman and pool phantoms (23). Contrast gain (%) was calculated as:

$$\frac{(Contrast_{TOF} - Contrast_{non-TOF}) \times 100}{Contrast_{non-TOF}}$$

where $Contrast_{TOF}$ and $Contrast_{non-TOF}$ are the contrast (%) with and without TOF, respectively.

These physical indices were calculated by PETquactIE ver. 3.0 (Nihon Medi-Physics CO., Ltd., Tokyo, Japan).

Clinical protocol

Data acquisition

The present study proceeded in accordance with the Declaration of Helsinki, and was approved by the Ethics Committee at the TMIG (Approval No. 28077). All controls and patients provided written informed consent to participate in the present study after physicians provided a detailed explanation of the study at the Research Team for Neuroimaging. The individuals rested comfortably in a quiet, dimly-lit room for several minutes, then were placed in the supine position for intravenous [¹⁸F]FDG injection and uptake. Low-dose CT images for attenuation and scatter correction were acquired before starting PET image acquisition. The first set of PMT-PET images were acquired for 10 min starting from 40 min after

[¹⁸F]FDG administration, then the second set of SiPM-PET images was acquired, also for 10 min. We started the second scan within 5 min of completing the first scan of 22 controls and 10 patients using two PET/CT scanners between April 2017 and July 2018. The controls were confirmed as not having degenerative neurological disorders on [¹⁸F]FDG and brain magnetic resonance images acquired using a Discovery MR750w 3.0T scanner (GE Healthcare). The MR images were acquired under the following conditions: three-dimensional mode (spoiled gradient recalled acquisition in the steady state: repetition time, 7.648 ms; echo time, 3.092 ms; matrix size, 196 × 256 × 256; voxel size, 1.2 × 1.0547 × 1.0547 mm³). Table 1 shows the characteristics of the controls. Four controls were healthy volunteers and 18 had visual issues (visual snow, n = 12; blepharospasm, n = 2; visual disturbance, n = 1; photophobia, n = 1; Charles Bonnet syndrome, n = 1; traffic injury, n = 1). Ten patients had suspected degenerative neurological disorders. Table 2 shows the characteristics of patients.

Data processing

We separately normalized [¹⁸F]FDG images of 22 controls to a standard [¹⁸F]FDG PET template using MIMneuro (MIM Software Inc. Cleveland, OH, USA). Anatomical volumes of interest (VOI) of MIMneuro were automatically placed on the caudate nucleus, cerebellum, frontal, occipital, parietal and temporal lobes, putamen, thalamus and whole brain. Mean standardized uptake values (SUV_{mean}) were measured using these VOIs (24). Images of the 22 controls and 10 patients were statistically analyzed using CortexID Suite (GE Healthcare) for (25-27). Anatomical VOI of CortexID Suite comprised the lateral and medial frontal, inferior and superior parietal, and lateral and medial temporal lobes, the anterior and posterior cingulate cortex, occipital lobe, sensorimotor, precuneus, primary visual cortex, and cerebellum. The SUV ratio (SUVR) was calculated using the value of the pons as a reference region. Z-scores for anatomical VOI-based analyses were calculated from anatomically normalized SUVR images using the formula,

$$\frac{(SUVR_{individual} - SUVR_{normal})}{SD_{normal}}$$

where $SUVR_{individual}$ and $SUVR_{normal}$ are the mean SUVR of the individuals and the normal database of CortexID Suite in the VOI, respectively and SD_{normal} is the SD of the SUVR of the normal database of

Data analyses

Data were statistically analyzed using GraphPad Prism 8 Version 8.4.0 (GraphPad Software Inc., San Diego, CA, USA). The SUV_{mean} of all regions for SiPM- and PMT- PET acquisitions were statistically compared using two-tailed paired Student t tests. Spearman rank correlation coefficients were calculated to evaluate relationships among different SUV_{mean} in the whole brain and intervals between acquisitions. Z-scores were statistically analyzed for both acquisitions using Wilcoxon matched-pairs signed rank tests. Values with $P < 0.05$ were considered significant.

Results

Phantom study

Table 3 shows that the physical indices of both scanners satisfied the JSNM image quality acceptance criteria of contrast $> 55\%$, $CV \leq 15\%$ and $SD \leq 0.0249$. The pool phantom images under the clinical conditions also satisfied the criterion of uniformity. Contrast was higher using SiPM-PET than PMT-PET. Contrasts were 70.0% for the SiPM-PET without TOF and 59.5% for the PMT-PET without TOF. The contrast in SiPM-PET was slightly improved using TOF.

Clinical study

Figure 1 and Table 4 show changes in SUV_{mean} and mean (\pm SD) SUV_{mean} across all brain regions of controls, respectively, between acquired using SiPM- and PMT-PET. The SUV_{mean} was significantly higher on SiPM-PET than PMT-PET images in all region. The mean (\pm SD) of the interval between sequential acquisitions (PMT-PET followed by SiPM-PET) was 15.2 ± 1.0 min for controls. The second acquisition started about 5 min after the end of the first acquisition. Figure 2 shows correlations between changes of SUV_{mean} in whole brain and time between first and second acquisitions in controls. The R of the SUV_{mean} was 0.06 ($P = 0.79$), then the SUV_{mean} was independent of the time.

Figure 3 shows that the comparisons of Z-scores that was analyzed using CotexID Suite in all regions (except the bilateral posterior cingulate) were significantly higher in SiPM-PET than PMT-PET images. Figure 4 shows [^{18}F]FDG images, Z-score maps, and MR images from a control who was a 71-year-old male with visual hallucinations and Charles Bonnet syndrome (CBS). Glucose metabolism was reduced at the visual association cortex, but hypermetabolism was undetectable on both statistical maps. Figure 5 shows [^{18}F]FDG images and Z-score maps from a 60-year-old female with suspected

frontotemporal lobar degeneration. Glucose metabolism was reduced at the left frontal, temporal, and parietal lobes, the precentral gyrus, striatum, and thalamus on both Z-score maps. The area of hypometabolism in statistical maps was reduced and localized by SiPM-PET compared with PMT-PET regardless of whether the images were derived from controls or patients (Figs. 4, 5, Supplements 1 and 2).

Discussion

We investigated the potential advantages of a new digital SiPM-PET/CT system, DMI, by head-to-head comparisons with a conventional PMT-PET/CT system, D710, in phantom and clinical studies using [^{18}F]FDG imaging. The SiPM-PET observed better contrast and uniformity than the PMT-PET and image noise of SiPM-PET was equivalent to the PMT-PET in phantom study. In clinical study, the SUV_{mean} was significantly higher on SiPM-PET than PMT-PET images in all region. Z-scores were significantly higher in SiPM-PET than PMT-PET images in all region except for the bilateral posterior cingulate.

The timing and spatial resolution is better for PET systems with SiPM than PMT (5, 6, 8, 9). The timing resolution is improved due to a bright scintillation crystal with short rise and/or decay times, a low height-width aspect ratio, and a peak emission wavelength that matches with the spectral sensitivity of the SiPM (28). The experimental detector system using SiPM has timing resolution of < 200 ps (7, 10). The clinical DMI PET system has a timing resolution of 375 ps. Other PET systems developed by Philips and Siemens have even shorter timing resolution at 322 ps and 214 ps, respectively, to use thinner scintillator crystals than our PET system (13, 29). The commercial clinical SiPM-PET have smaller crystals (< 4.0 mm) than PMT-PET (13, 17, 29). The SiPM-PET detector improved the ability to detect small lesions, and its features can be summarized as better spatial resolution, timing resolution, and sensitivity compared with conventional PMT-PET (16-18).

Contrast was better in the phantom images acquired using SiPM-PET than PMT-PET and slightly improved when using SiPM-PET with TOF. The contrast in this study was better than that we previously reported in which we measured radioactivity of the Hoffman phantom using a 1-cm circular region of interest (ROI) (17). We used a JSNM ROI template that covers regions of gray and white matter in the present study, which suppressed spillover from white matter and increased contrast (23). The true radioactive distribution ratio in Hoffman phantom mimicking the cerebral blood flow ratio of gray and white matter is 4. However, the gray to white matter contrast measured on PET images was degenerated

by partial volume effects (PVE). The SiPM-PET with a crystal size of < 4 mm decreased PVE and achieved better contrast than PMT-PET. The images of a larger matrix also reduce PVE in PET images. We reconstructed Hoffman phantom images using 256 × 256 matrix with 1-mm pixels and evaluated physical indices (supplement 3). The contrast was essentially the same between SiPM-PET with a large matrix and clinical conditions (72.8% vs. 72.4%). The ultimate spatial resolution was calculated as:

$$\Gamma = \sqrt{(d/2)^2 + s^2 + (0.0044R)^2} ,$$

where Γ is the spatial resolution (mm), d is the crystal width, s is the positron range, and R is the detector ring radius (12). Thus, the ultimate spatial resolution never fell below $d/2$. The respective detector widths are 3.95 and 4.2 mm for SiPM-PET and PMT-PET. We believe that the 128 × 128 matrix with 2-mm pixels are valid for clinical applications. The improvement in image contrast (23.8%) using SiPM-PET in present study was smaller than that in the clinical study of the Philips SiPM-PET because they had smaller scintillator crystals than those in our detector (20). However, they did not find a benefit of TOF with an SiPM-PET system for brain PET. Nagaki et al. found that contrast in [¹⁸F]FDG brain imaging was not improved using the PMT-PET system at a timing resolution of 555 ps (30). The sensitivity gain using TOF was increased as a function of increasing the object size (31). The timing resolution of SiPM-PET and PMT-PET was 375 and 544 ps, respectively (16, 21). These led to spatial localization along a line of response of 5.8 and 7.5 cm, respectively (17). We considered that the SiPM-PET with TOF would improve image contrast more in brain PET images, but it was actually slight. Sluit et al. showed clear demarcation of the striatum and thalamus using a Siemens SiPM-PET with a timing resolution of 214 ps (13). Yoshida et al. developed a brain-dedicated PET system with timing resolution of 245 ps and generated high-quality images from the Hoffman phantom (32), but did not investigate the benefit of SiPM-PET with TOF using physical indices in brain imaging. We previously generated visually improved [¹⁸F]FDG brain images using SiPM-PET with TOF (17). Sluis et al. evaluated the performance of a Siemens SiPM-PET using NEMA tests and visually compared [¹⁸F]FDG brain images acquired by PMT-PET and SiPM-PET, but did not physically evaluate the quality of [¹⁸F]FDG brain images (13). The benefit of TOF with a timing resolution of < 300 ps should be investigated in the future.

Image noise was the same between SiPM-PET and PMT-PET in the present study, although a wider axial FOV contributed to the better sensitivity of DMI compared with the D710 (200 vs. 157 mm) (17). The statistical noise at the center slice was higher in SiPM-PET than PMT-PET images because the DMI slices were thinner than those of D710 (2.79 vs. 3.27 mm). The SiPM-PET did not improve the statistical noise under the clinical conditions of 20 MBq of radioactivity and an acquisition duration of 7 min. There is trade-off between the sensitivity and timing resolution in SiPM-PET. Smaller crystals used to reduce timing resolution also reduce sensitivity (28, 32). The sensitivity was equivalent between the DMI with 3 detector rings (axial FOV, 150 mm) and the D710 (axial FOV, 157 mm) (33, 34). Thus, we argue that the optimal method to reduce image noise in SiPM-PET is to increase the detector ring to extend the axial FOV.

The phantom images acquired by SiPM-PET had better uniformity. The SD was calculated from the mean radioactivity concentration at the center slice and on the slice ± 40 mm from the center of the pool phantom that corresponded to the cerebellum (- 40 mm) and parietal lobe (+ 40 mm) in the human brain (23). Uniformity can be estimated as an index of the count stability through the entire axial FOV. Good uniformity means the less statistical noise on PET image at the edge of axial FOV. The SiPM-PET could include a whole brain within its PET axial FOV. The statistical noise was suppressed at the bottom of the brain such as pons and cerebellum where were the reference region to calculate the SUVR for [^{18}F]FDG (24), amyloid (35, 36), and Tau (37) PET imaging using the SiPM-PET. Therefore, the SUVR calculated by SiPM-PET was expected to be stable.

The clinical study showed that the SUV_{mean} was significantly higher using SiPM-PET than PMT-PET and did not correlate with the delay of the time from the injection (38). The superior spatial resolution by SiPM-PET not only improved image contrast but also increased the SUV_{mean} in the cortex (39). The higher Z-scores determined using SiPM-PET was affected by higher SUV_{mean} . CortexID Suite uses the three-dimensional stereotactic surface projections (3D-SSP) as a method of statistical image analysis (25). The SiPM-PET raised the peak signal on the cortex that was used to analyze the 3D-SSP because small scintillator crystals in the SiPM-PET reduced PVEs in the signal of gray matter (16). Salvadori et al. also found better recovery coefficient in SiPM-PET than PMT-PET even if same pixel size (20). On the other hand, the Japanese Alzheimer Disease Neuroimaging Initiative study found higher [^{18}F]FDG distribution

in late- (55 – 60 min) than in early- (30 – 35 min) scans of the frontal and parietal lobes (40). We also found a higher SUV_{mean} in the second, compared with the first scan of the frontal and parietal lobes. However, the difference in SUV_{mean} in these lobes did not correlate with elapsed time from injection. We argue that the SiPM-PET contributes to improving signal loss resulting from PVE in brain PET imaging.

Significant hypometabolism was detected in the primary visual cortex and visual association cortex on Z-score maps (Fig. 5D and E). Charles Bonnet syndrome appeared as hypometabolism in the primary visual cortex and hypermetabolism in the visual association cortex on $[^{18}F]FDG$ PET images (41). Hypermetabolism was undetectable in the visual association cortex because this person might have had fewer or milder symptoms of CBS than visual hallucinations. The statistical hypometabolic areas in Z-score maps of controls and patients were reduced and localized by SiPM-PET. The SiPM-PET improved the PVE and expressed truer metabolic distribution than PMT-PET. Misdiagnosis in dementia corrected using 3D-SSP has significantly enhanced the diagnostic confidence of nuclear medicine physicians (42). False positive findings in the CortexID Suite can be reduced using SiPM-PET. Thus, $[^{18}F]FDG$ images acquired using SiPM-PET will help to improve diagnostic outcomes based on statistical image analysis.

The present study has some limitations. We initially investigated a few patients with neurological disorders. The tendency for Z-scores and hypometabolic areas to differ between SiPM- and PMT-PET images of patients with neurological disorders and controls was equivalent. The detectability and diagnostic performance of patients with neurological disorders should be assessed in a larger population of $[^{18}F]FDG$ brain images using SiPM-PET. Secondly, twice acquisitions using SiPM- and PMT-PET were performed in specific order. The sequential acquisition in inverse order should be performed to observe the actual change of SUV, although the SUV did not correlate with the delay of the time from the injection in present study. Thirdly, the normal $[^{18}F]FDG$ database in the CortexID Suite does not include image data acquired by more recent PET scanners such as SiPM-PET. The diagnostic performance of the CortexID Suite would certainly improve with an updated normal database.

Conclusions

The improved spatial resolution and sensitivity of SiPM-PET contributed to better image contrast and uniformity in brain $[^{18}F]FDG$ images. The SiPM-PET offers better quality and more accurate quantitation of brain PET images. The SUV_{mean} and Z-score in SiPM-PET was higher than PMT-PET due to improving the PVEs. $[^{18}F]FDG$ images acquired using SiPM-PET will help to improve diagnostic outcomes based on

statistical image analysis because the SiPM-PET would localize the distribution of glucose metabolism on Z-score maps.

List Of Abbreviations

[¹⁸F]FDG, ¹⁸F-fluoro-2-deoxy-D-glucose

3D-OS-EM, Three dimensional-Ordered Subset-Expectation Maximization

3D-SSP, Three-dimensional stereotactic surface projections

AD, Alzheimer disease

CT, Computed tomography

CV, Coefficient of variation

D710, Discovery PET/CT 710

DMI, Discovery MI

FOV, Field-of-view

FTLD, Frontotemporal lobar degeneration

FWHM, Full width at half maximum

Hoffman phantom, Hoffman 3D brain phantom

JSNM, Japanese Society of Nuclear Medicine

L, Left

LBS, Lutetium based scintillators

MCI, mild cognitive impairment

NEMA, National Electrical Manufactured Association

No., Number

PET, Positron emission tomography

PMT, Photomultiplier tubes

Pt., Patients

R, Right

ROI, Region of interest

SD, Standard deviation

SiPM, Silicon photomultiplier

SUV_{mean}, Mean standardized uptake value

SUVR, SUV ratio

TMIG, Tokyo Metropolitan Institute of Gerontology

TOF, Time-of-flight

VOI, Volume of interest

Declarations

Ethics approval and consent to participate and Consent for publication

The present study proceeded in accordance with the Declaration of Helsinki, and was approved by the Ethics Committee at the TMIG (Approval No. 28077). All applicants provided written informed consent to participate in the present study after physicians provided a detailed explanation of the study.

Availability of data and material

All data generated and analyzed during this study are included in this published article.

Competing interests

AH and HK are employed by GE Healthcare. KW, SM, and K Ishii were supported a research grant from GE Healthcare.

Funding

The design of the study, collection and analysis were supported by a research grant from GE Healthcare.

Authors' contributions

KW, AH, HK, and K Ishii designed the study. KW, K Ishibashi, YS, and K Ishii collected the data. KW and MS processed the data. KW, MS, KM, and K Ishii interpreted the data. KW drafted and revised the manuscript. All authors read and approved the final version of the manuscript.

Acknowledgements

We thank Mr. Shotaro Yamaguchi for technical support with the phantom experiment, Mr. Kunpei Hayashi and Mr. Masanari Sakai for technical support with the cyclotron operation and radiosynthesis, and Ms. Kimiko Yokoyama and Mr. Kazuno Hino for patient care as they underwent PET.

References

1. Wahl RL, Jacene H, Kasamon Y, Lodge MA. From RECIST to PERCIST: Evolving Considerations for PET response criteria in solid tumors. *J Nucl Med*. 2009;50(Suppl 1):122S-50S.
2. Herholz K, Westwood S, Haense C, Dunn G. Evaluation of a calibrated (18)F-FDG PET score as a biomarker for progression in Alzheimer disease and mild cognitive impairment. *J Nucl Med*. 2011;52(8):1218-26.
3. Foster NL, Heidebrink JL, Clark CM, Jagust WJ, Arnold SE, Barbas NR, et al. FDG-PET improves accuracy in distinguishing frontotemporal dementia and Alzheimer's disease. *Brain*. 2007;130(Pt 10):2616-35.
4. Rabinovici GD, Rosen HJ, Alkalay A, Kornak J, Furst AJ, Agarwal N, et al. Amyloid vs FDG-PET in the differential diagnosis of AD and FTL. *Neurology*. 2011;77(23):2034-42.
5. Kataoka J, Kishimoto A, Fujita T, Nishiyama T, Kurei Y, Tsujikawa T, et al. Recent progress of MPPC-based scintillation detectors in high precision X-ray and gamma-ray imaging. *Nuclear Instruments and Methods in Physics Research Section A: Accelerators, Spectrometers, Detectors and Associated Equipment*. 2015;784:248-54.
6. David S, Georgiou M, Fysikopoulos E, Loudos G. Evaluation of a SiPM array coupled to a Gd₃Al₂Ga₃O₁₂:Ce (GAGG:Ce) discrete scintillator. *Phys Med*. 2015;31(7):763-6.
7. Huizenga J, Seifert S, Schreuder F, van Dam HT, Dendooven P, Löhner H, et al. A fast preamplifier concept for SiPM-based time-of-flight PET detectors. *Nuclear Instruments and Methods in Physics Research Section A*. 2012;695:379-84.
8. Levin CS, Maramraju SH, Khalighi MM, Deller TW, Delso G, Jansen F. Design Features and Mutual Compatibility Studies of the Time-of-Flight PET Capable GE SIGNA PET/MR System. *IEEE Trans Med Imaging*. 2016;35(8):1907-14.
9. Peng H, Levin LC. Recent Developments in PET Instrumentation. *Curr Pharm Biotechnol*. 2010;11(6):555-71.
10. Schaart DR, Seifert S, Vinke R, van Dam HT, Dendooven P, Löhner H, et al. LaBr₃:Ce and SiPMs for time-of-flight PET: achieving 100 ps coincidence resolving time. *Phys Med Biol*. 2010;55(7):N179-89.
11. Slomka PJ, Pan T, Germano G. Recent Advances and Future Progress in PET Instrumentation. *Semin Nucl Med*. 2016;46(1):5-19.
12. Moses WW. Fundamental limits of spatial resolution in PET. *Nucl Instrum Methods Phys Res A*. 2011;648(Supplement 1):S236-40.

13. van Sluis J, Boellaard R, Somasundaram A, van Snick P, Borra R, Dierckx R, et al. Image Quality and Semiquantitative Measurements on the Biograph Vision PET/CT System: Initial Experiences and Comparison with the Biograph mCT. *J Nucl Med.* 2020;61(1):129-35.
14. Buzhan P, Dolgoshein B, Ilyin A, Kantserov V, Kaplin V, Karakash A, et al. AN ADVANCED STUDY OF SILICON PHOTOMULTIPLIER. *Advanced Technology and Particle Physics.* 2002:717-28.
15. Buzhan P, Dolgoshein B, Filatov L, Ilyin A, Kantzerov V, Kaplin V, et al. Silicon photomultiplier and its possible applications. *Nuclear Instruments and Methods in Physics Research Section A.* 2003;504(1-3):48-52.
16. Hsu DF, Ilan E, Peterson WT, Uribe J, Lubberink M, Levin CS. Studies of a Next-Generation Silicon-Photomultiplier-Based Time-of-Flight PET/CT System. *J Nucl Med.* 2017;58(9):1511-8.
17. Wagatsuma K, Miwa K, Sakata M, Oda K, Ono H, Kameyama M, et al. Comparison between new-generation SiPM-based and conventional PMT-based TOF-PET/CT. *Phys Med.* 2017;42:203-10.
18. Aljared A, Alharbi AA, Huellner MW. BSREM Reconstruction for Improved Detection of In-Transit Metastases With Digital FDG-PET/CT in Patients With Malignant Melanoma. *Clin Nucl Med.* 2018;43(5):370-1.
19. Sonni I, Baratto L, Park S, Hatami N, Srinivas S, Davidzon G, et al. Initial experience with a SiPM-based PET/CT scanner: influence of acquisition time on image quality. *EJNMMI Phys.* 2018;5(1):9.
20. Salvadori J, Imbert L, Perrin M, Karcher G, Lamiral Z, Marie PY, et al. Head-to-head comparison of image quality between brain ^{18}F -FDG images recorded with a fully digital versus a last-generation analog PET camera. *EJNMMI Res.* 2019;9(1):61.
21. Bettinardi V, Presotto L, Rapisarda E, Picchio M, Gianolli L, Gilardi MC. Physical performance of the new hybrid PETCT Discovery-690. *Med Phys.* 2011;38(10):5394-411.
22. Hoffman EJ, Cutler PD, Guerrero TM, Digby WM, Mazziotta JC. Assessment of accuracy of PET utilizing a 3-D phantom to simulate the activity distribution of [^{18}F]fluorodeoxyglucose uptake in the human brain. *J Cereb Blood Flow Metab.* 1991;11(2):A17-25.
23. Akamatsu G, Ikari Y, Nishio T, Nishida H, Ohnishi A, Aita K, et al. Optimization of image reconstruction conditions with phantoms for brain FDG and amyloid PET imaging. *Ann Nucl Med.* 2016;30(1):18-28.
24. Partovi S, Yuh R, Pirozzi S, Lu Z, Couturier S, Grosse U, et al. Diagnostic performance of an automated analysis software for the diagnosis of Alzheimer's dementia with ^{18}F FDG PET. *Am J Nucl Med Mol Imaging.* 2017;7(1):12-23.
25. Minoshima S, Frey KA, Koeppe RA, Foster NL, Kuhl DE. A diagnostic approach in Alzheimer's disease using three-dimensional stereotactic surface projections of fluorine-18-FDG PET. *J Nucl Med.* 1995;36(7):1238-48.
26. Josephs KA, Duffy JR, Strand EA, Machulda MM, Senjem ML, Master AV, et al. Characterizing a neurodegenerative syndrome: primary progressive apraxia of speech. *Brain.* 2012;135(Pt 5):1522-36.
27. Probasco JC, Solnes L, Nalluri A, Cohen J, Jones KM, Zan E, et al. Abnormal brain metabolism on FDG-PET/CT is a common early finding in autoimmune encephalitis. *Neurol Neuroimmunol*

- Neuroinflamm. 2017;4(4):e352.
28. Yeom JY, Vinke R, Levin CS. Optimizing timing performance of silicon photomultiplier-based scintillation detectors. *Phys Med Biol.* 2013;58(4):1207-20.
 29. Zhang J, Maniawski P, Knopp MV. Performance evaluation of the next generation solid-state digital photon counting PET/CT system. *EJNMMI Res.* 2018;8(1):97.
 30. Nagaki A, Onoguchi M, Matsutomo N. Clinical validation of high-resolution image reconstruction algorithms in brain ^{18}F -FDG-PET: effect of incorporating Gaussian filter, point spread function, and time-of-flight. *Nucl Med Commun.* 2014;35(12):1224-32.
 31. Surti S. Update on time-of-flight PET imaging. *J Nucl Med.* 2015;56(1):98-105.
 32. Yoshida E, Tashima H, Akamatsu G, Iwao Y, Takahashi M, Yamashita T, et al. 245 ps-TOF brain-dedicated PET prototype with a hemispherical detector arrangement. *Phys Med Biol.* 2020. [Epub ahead of print].
 33. Levin C, Peterson W, Ross S, Stearns C, Uribe J. PET performance as a function of axial field of view for a new silicon photomultiplier-based whole body TOF PET/CT system. *J Nucl Med.* 2016;57(Suppl. 2):200.
 34. Pan T, Einstein SA, Kappadath SC, Grogg KS, Gomez CL, Alessio AM, et al. Performance evaluation of the 5-Ring GE Discovery MI PET/CT system using the national electrical manufacturers association NU 2-2012 Standard. *Med Phys.* 2019;46(7):3025-33.
 35. Joshi AD, Pontecorvo MJ, Lu M, Skovronsky DM, Mintun MA, Devous MD, Sr. A Semiautomated Method for Quantification of F 18 Florbetapir PET Images. *J Nucl Med.* 2015;56(11):1736-41.
 36. Nelissen N, Van Laere K, Thurfjell L, Owenius R, Vandenbulcke M, Koole M, et al. Phase 1 study of the Pittsburgh compound B derivative ^{18}F -flutemetamol in healthy volunteers and patients with probable Alzheimer disease. *J Nucl Med.* 2009;50(8):1251-9.
 37. Barret O, Alagille D, Sanabria S, Comley RA, Weimer RM, Borroni E, et al. Kinetic Modeling of the Tau PET Tracer ^{18}F -AV-1451 in Human Healthy Volunteers and Alzheimer Disease Subjects. *J Nucl Med.* 2017;58(7):1124-31.
 38. Baratto L, Park SY, Hatami N, Davidzon G, Srinivas S, Gambhir SS, et al. ^{18}F -FDG silicon photomultiplier PET/CT: A pilot study comparing semi-quantitative measurements with standard PET/CT. *PLoS One.* 2017;12(6):e0178936.
 39. Lindström E, Sundin A, Trampal C, Lindsjö L, Ilan E, Danfors T, et al. Evaluation of Penalized-Likelihood Estimation Reconstruction on a Digital Time-of-Flight PET/CT Scanner for ^{18}F -FDG Whole-Body Examinations. *J Nucl Med.* 2018;59(7):1152-8.
 40. Takahashi R, Ishii K, Senda M, Ito K, Ishii K, Kato T, et al. Equal sensitivity of early and late scans after injection of FDG for the detection of Alzheimer pattern: an analysis of 3D PET data from J-ADNI, a multi-center study. *Ann Nucl Med.* 2013;27(5):452-9.
 41. Garde N Skripuletz T, Pul R, Berding G, Weissenborn K, Trebst C. Visual Hallucinations in Charles Bonnet Syndrome Can Be Seen in Fluorodeoxyglucose-PET. *J Neuropsychiatry Clin Neurosci.*

2011;23(4):E38-9.

42. Kim J, Cho SG, Song M, Kang SR, Kwon SY, Choi KH, et al. Usefulness of 3-dimensional stereotactic surface projection FDG PET images for the diagnosis of dementia. *Medicine (Baltimore)*. 2016;95(49):e5622.

Supplementary File Legend

Supplement 1. Z-score maps of bilateral and bimedial images in 22 controls.

The color scale is -7.0 to 0.0 of Z-score. PET, positron emission tomography. PMT, photomultiplier tubes; SiPM, silicon photomultiplier.

Supplement 2. Z-score maps of bilateral and bimedial images in 10 patients.

The color scale is -7.0 to 0.0 of Z-score.

Tables

Table 1. Characteristics of controls (n = 22)

Age (mean \pm SD, range)	41.1 \pm 18.9, (21 - 75)
Male (n)	11
Height (cm)	166.1 \pm 7.5
Weight (kg)	58.5 \pm 9.1
Glucose (mg/dL)	101.0 \pm 13.7
Injected dose (MBq)	155.8 \pm 14.7
Uptake duration (min, PMT-PET/SiPM-PET)	40.1 \pm 0.6/55.3 \pm 1.2

Data are shown as means \pm standard deviation. PET, positron emission tomography; PMT, photomultiplier tube; SiPM, Silicon photomultiplier.

Table 2. Characteristics of patients

Pt.	Clinical diagnosis	Age	Sex	Weight (kg)	Glucose (mg/dL)	Injected dose (MBq)	Uptake duration (min, PMT/SiPM)
1	MCI	72	Male	63.3	96	162.5	40.0/55.6
2	Amnesia	49	Male	73.1	102	151.7	40.0/54.5
3	FTLD	60	Female	63.0	95	149.3	40.0/57.5
4	Juvenile AD	49	Male	89.4	93	168.7	40.0/57.2
5	Juvenile AD	55	Male	65.4	111	172.1	40.0/56.8
6	MCI	70	Female	46.6	90	174.8	40.1/56.6
7	Amnesia, AD	81	Male	55.5	96	165.0	40.0/55.6
8	Dystonia	36	Female	42.9	99	172.2	40.0/54.7
9	Familial AD	55	Female	54.0	96	160.4	40.0/54.5
10	Posterior cortical atrophy	63	Male	61.3	100	140.1	40.0/57.0
Means ± SD	-	59.0 ±13.1	-	61.5 ± 13.3	97.8 ± 5.8	161.7 ±11.4	40.0 ± 0.0/ 56.0 ± 1.2

AD, Alzheimer disease; FTLD, frontotemporal lobar degeneration; MCI, mild cognitive impairment; PMT, photomultiplier tube; SiPM, Silicon photomultiplier.

Table 3. Physical indices in JSNM criteria and contrast gain in background of SiPM- and PMT-PET.

PET system	Contrast (%)	CV (%)	SD	(clinical vs. 30 min)	Contrast gain (%)
PMT-PET	58.5	11.1	0.021/0.018		-1.7
SiPM-PET	72.4	11.5	0.015/0.009		3.5

JSNM criteria: contrast ratio > 55%, CV < 13%, SD < 0.0249. CV, coefficient of variation; JSNM, Japanese Society of Nuclear Medicine; PET, positron emission tomography; PMT, photomultiplier tube; SD, standard deviation; SiPM, silicon photomultiplier.

Table 4. Mean standardized uptake values for [¹⁸F]FDG brain images acquired using SiPM- and PMT-PET (n = 22).

Region	PMT-PET	SiPM-PET	Difference
Cerebellum	5.5 ± 0.7	5.9 ± 0.7	7.9%
Brain stem	4.4 ± 0.5	4.6 ± 0.5	5.4%
Caudate	6.8 ± 1.3	7.4 ± 1.3	8.6%
Frontal lobe	6.6 ± 1.0	7.4 ± 1.1	11.0%
Occipital lobe	6.5 ± 0.9	7.5 ± 1.0	14.1%
Parietal lobe	6.2 ± 0.9	6.9 ± 1.0	11.9%
Temporal lobe	5.8 ± 0.8	6.6 ± 0.9	14.2%
Putamen	7.8 ± 1.1	8.5 ± 1.1	9.3%
Thalamus	6.9 ± 1.1	7.4 ± 1.1	7.2%
Whole brain	5.5 ± 0.8	6.1 ± 0.8	11.0%

Data are shown as means ± standard deviation. PET, positron emission tomography; PMT, photomultiplier tube; SiPM, Silicon photomultiplier.

Figures

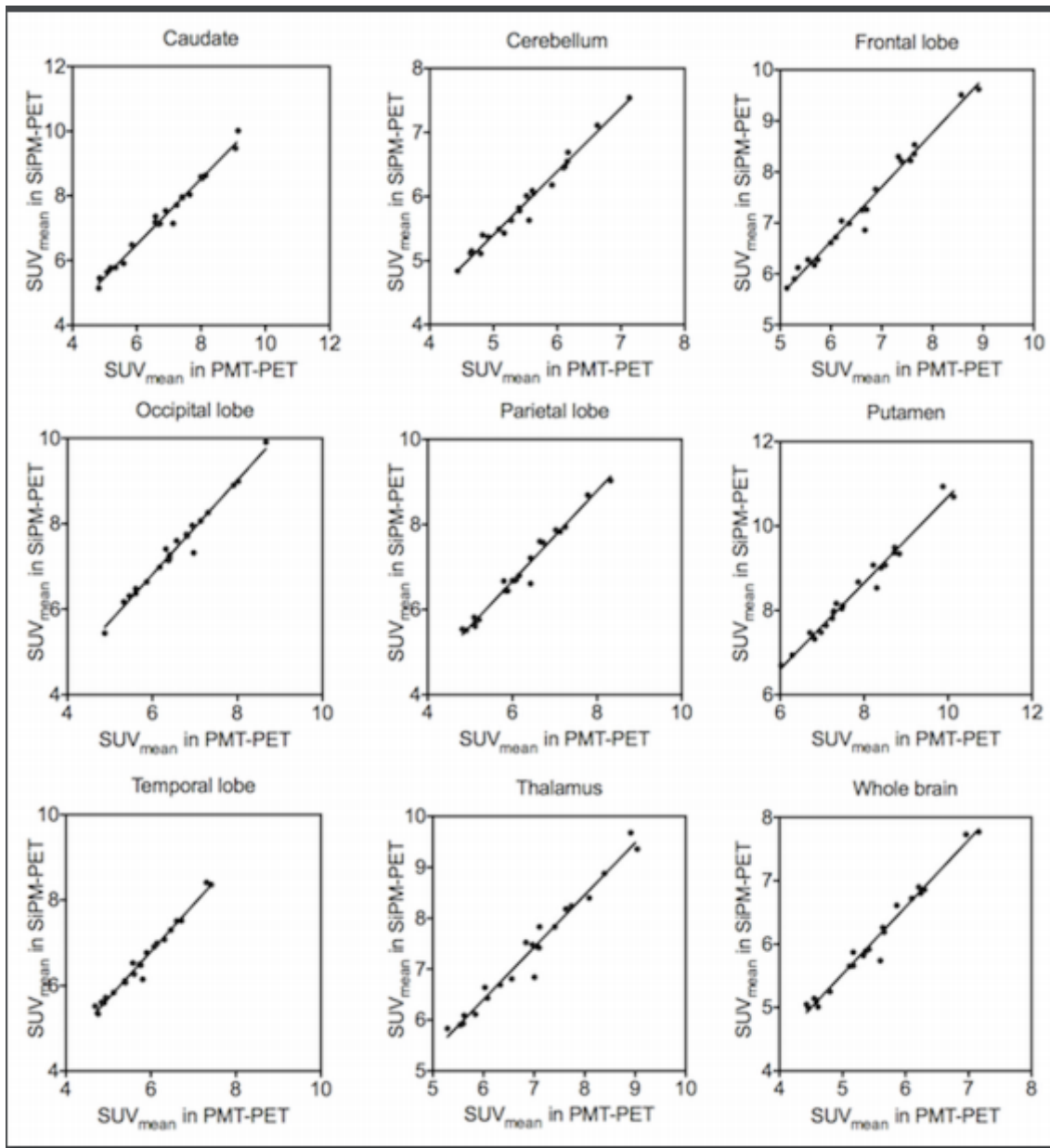


Figure 1

Changes in SUV_{mean} of all regions in images acquired by PMT-PET and SiPM-PET. PET, positron emission tomography; PMT, photomultiplier tube; SiPM, silicon photomultiplier; SUV_{mean}, mean standardized uptake value.

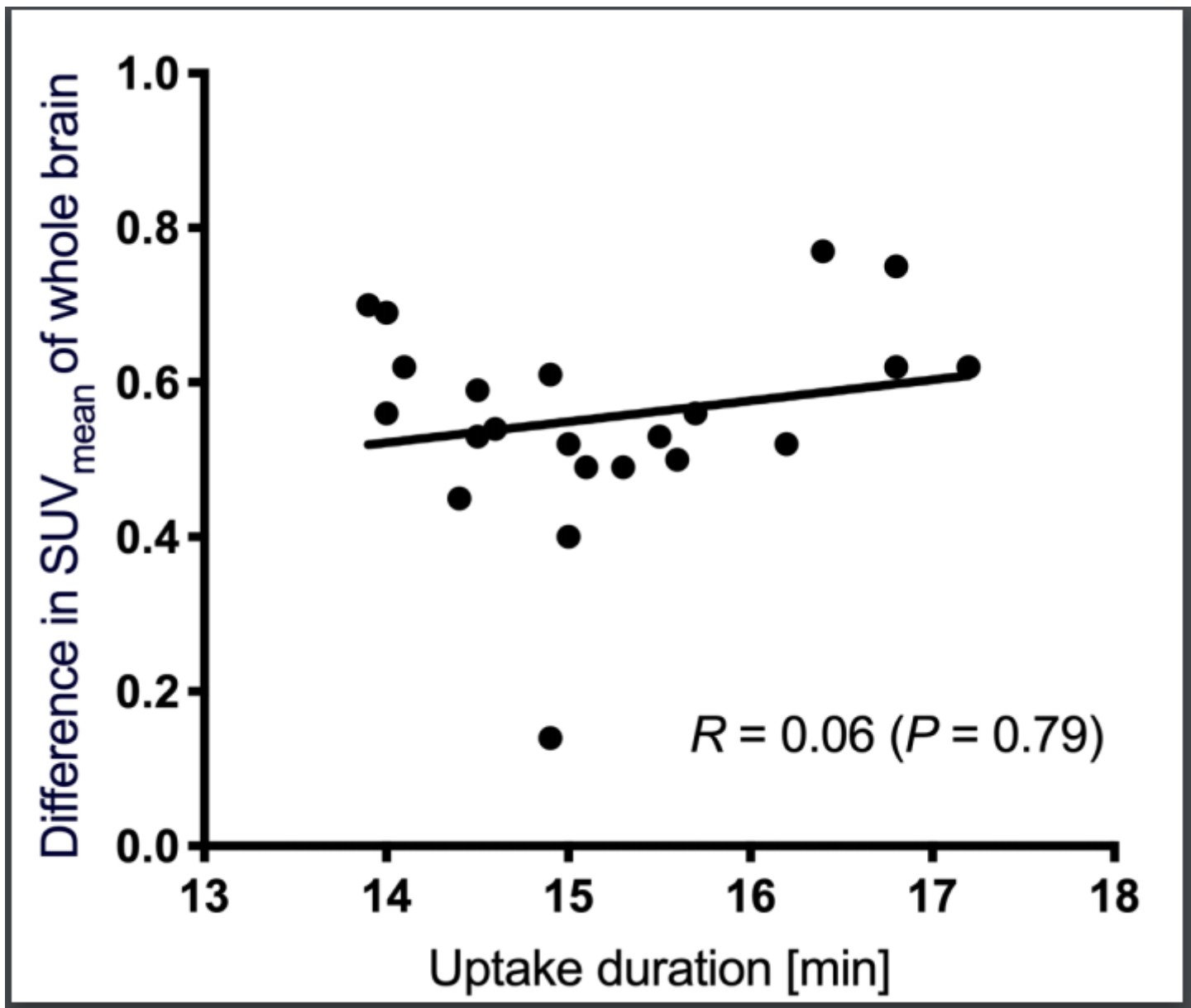


Figure 2

Correlations between changes in SUV_{mean} in whole brain and all regions and time between sequential acquisitions. SUV_{mean}, mean standardized uptake value.

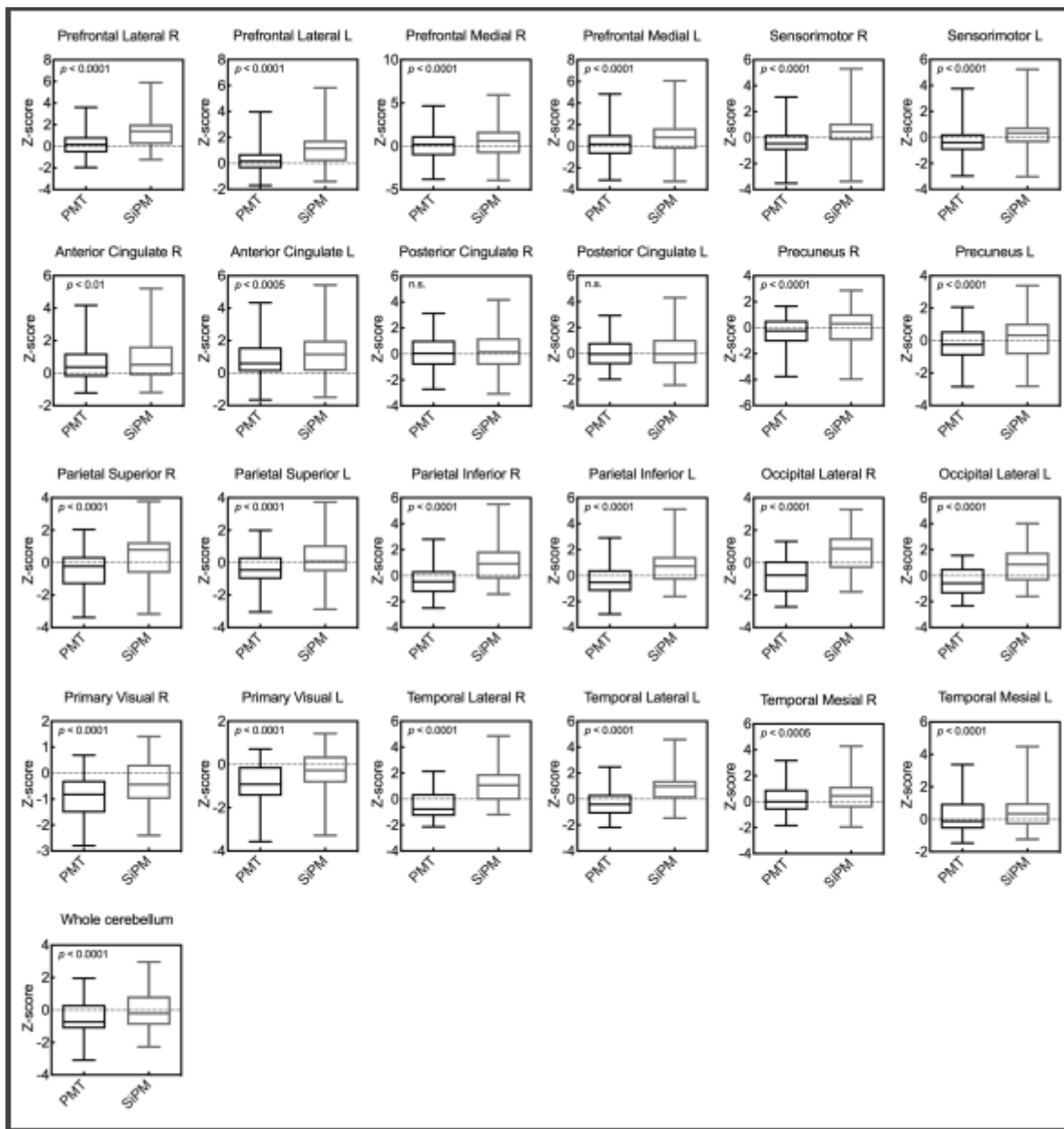


Figure 3

Z-scores in all brain regions in PMT-PET and SiPM-PET images. L, left; PET, positron emission tomography. PMT, photomultiplier tube; R, right; SiPM, silicon photomultiplier.

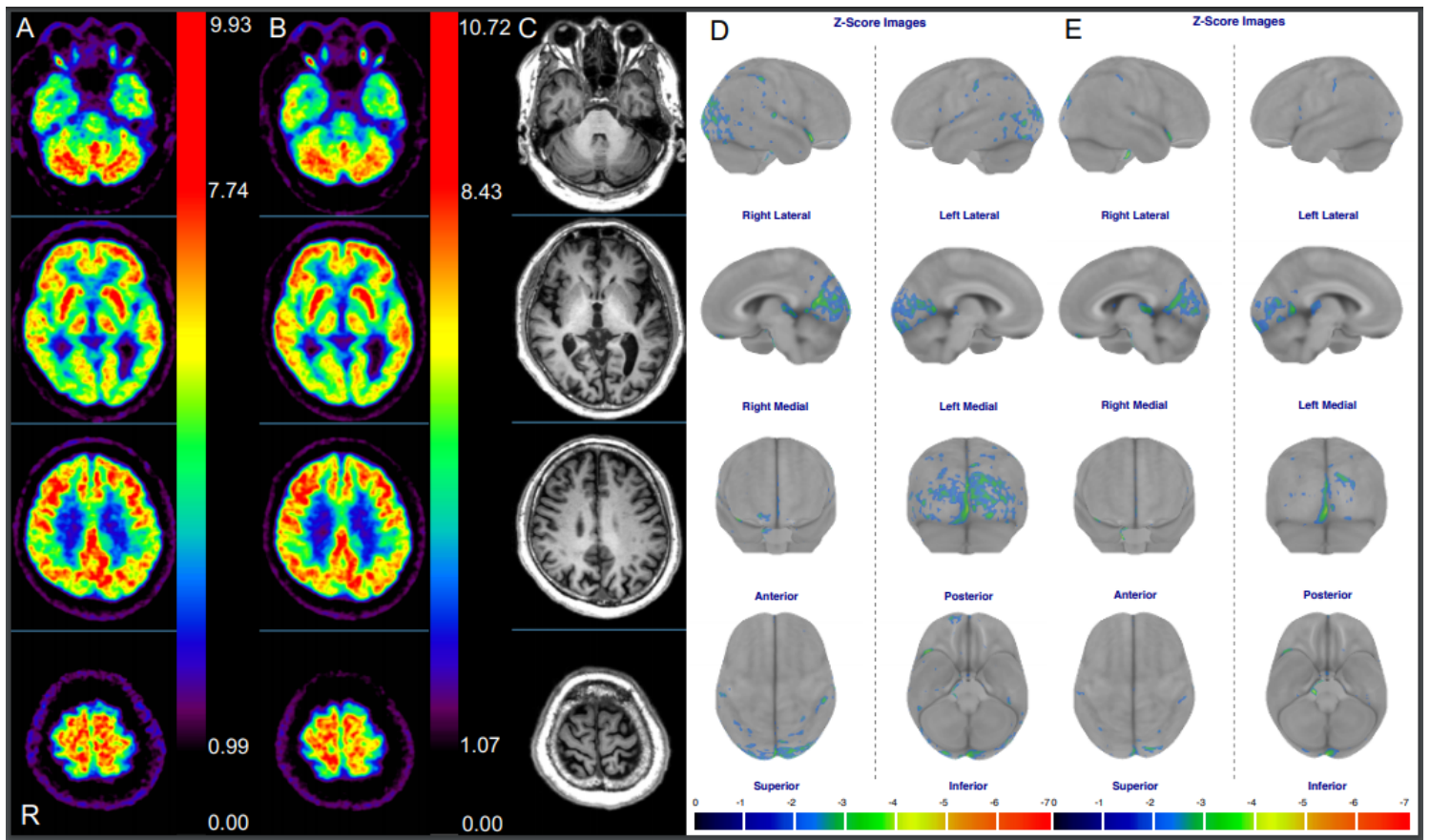


Figure 4

[¹⁸F]FDG images, MR images, and Z-score maps derived from a 71-year-old male. [¹⁸F]FDG images acquired using PMT-PET (A) and SiPM-PET (B). MR image of slices of both [¹⁸F]FDG images (C). Z-score maps calculated from PMT-PET (D) and SiPM-PET (E) images. MR, magnetic resonance; PET, positron emission tomography; PMT, photomultiplier tube; SiPM, silicon photomultiplier.

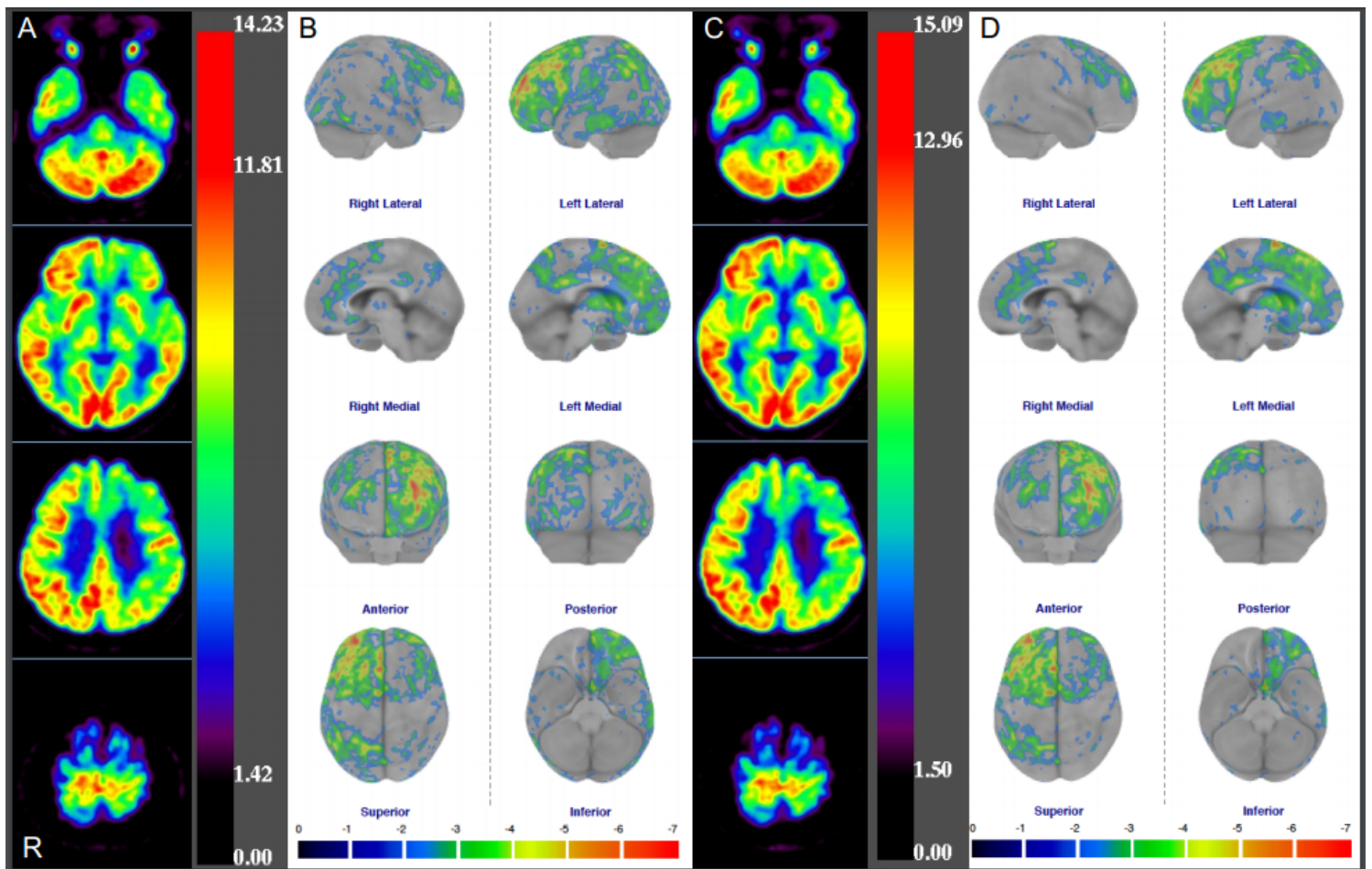


Figure 5

[18F]FDG images and Z-score maps derived from a 60-year-old female with suspected frontotemporal lobar degeneration. [18F]FDG images (A) and Z-score maps (B) in PMT-PET and [18F]FDG images (C) and Z-score maps (D) in SiPM-PET. PET, positron emission tomography; PMT, photomultiplier tube; SiPM, silicon photomultiplier.

Supplementary Files

This is a list of supplementary files associated with this preprint. Click to download.

- [Supplement1R1.pdf](#)
- [Supplement2R1.pdf](#)
- [Supplement3R1.docx](#)